Journal of Alloys and Compounds 509S (2011) S633–S639

Contents lists available at ScienceDirect

Journal of Alloys and Compounds

journal homepage: www.elsevier.com/locate/jallcom

Microstructural optimization of $LaMg_{12}$ alloy for hydrogen storage

Andrey A. Poletaev[a,b,1], Roman V. Denys[a,c], Jan Ketil Solberg[b], Boris P. Tarasov[d], Volodymyr A. Yartys[a,b,*]

[a] Institute for Energy Technology, Kjeller, NO 2027, Norway
[b] Department of Materials Science and Engineering, Norwegian University of Science and Technology, Trondheim, NO 7491, Norway
[c] Karpenko Physico-Mechanical Institute, National Academy of Sciences of Ukraine, L'viv 79601, Ukraine
[d] Institute of Problems of Chemical Physics of the Russian Academy of Sciences, Chernogolovka 142432, Russia

ARTICLE INFO

Article history:
Received 16 August 2010
Received in revised form
21 September 2010
Accepted 26 September 2010
Available online 2 October 2010

Keywords:
Magnesium: Lanthanum
Metal hydride
Hydrogen metallurgy
Rapid Solidification
Synchrotron diffraction
Crystal structure

ABSTRACT

A Rapid Solidification technique was applied to a $LaMg_{12}$ alloy in order to achieve refinement of the grain size. Thin ribbons were produced by solidifying the melt on a spinning copper wheel in an argon atmosphere using three different rotations speeds, 3.1, 10.5 and 20.9 m/s. The ribbons were analyzed by synchrotron X-ray diffraction (SR XRD), electron probe microanalysis (EPMA), and TEM, and they were subjected to hydrogen absorption–desorption cycling and to thermal desorption spectroscopy (TDS) characterization. SR XRD and EPMA revealed formation of two phases, $LaMg_{12-x}$ and Mg. From SR XRD it was found that, depending on the cooling rate, the $LaMg_{12-x}$ alloy crystallized with three different structural modifications, hexagonal $TbCu_7$ (highest cooling rate), tetragonal $ThMn_{12}$ (medium cooling rate) and orthorhombic $LaMg_{11}$ type (lowest cooling rate). A metastable $TbCu_7$-type structure (sp. gr. *P6/mmm*; $a = 5.9617(3)$; $c = 5.2153(5)$ Å) was not known from the earlier performed research and is reported for the La–Mg system for the first time. From the scanning electron microscopy (SEM) studies, RS was found to cause a significant grain refinement and an amorphisation for the highest cooling rate. The particle size of the formed hydride phases varied in the range 0.2–3 μm depending on the RS synthesis route used to prepare the original alloy. Hydrogen absorption resulted in a two-step disproportionation process: $LaMg_{12} + H_2 \rightarrow LaH_3 + Mg \rightarrow LaH_3 + MgH_2$. A decrease in the grain size improved the hydrogenation kinetics. Hydrogen desorption studied by TDS and *in situ* SR XRD showed a major peak of hydrogen evolution at ~370 °C. For the alloys synthesized at 10.5 m/s and 20.9 m/s, it was accompanied by an extra desorption event at 415 °C. This extra peak was associated with Mg-assisted low temperature hydrogen desorption from LaH_2 proceeding below 450 °C and leading to a recombination process to form the initial intermetallic alloy $LaMg_{12}$.

1. Introduction

Several classes of La-containing Mg-based intermetallic compounds have been studied as hydrogen storage materials. These include Mg-rich $LaMg_{12}$ [1–3] and La_2Mg_{17} [2]. High hydrogenation temperatures, repeated cycling of H absorption and desorption, application of reactive ball milling in hydrogen atmosphere and long interaction times are required to achieve high/complete hydrogenation of $LaMg_{12}$ [4–6]. As the $LaMg_{12\pm x}$ intermetallic has a broad homogeneity range from $x = -1.2$ to $x = 1.0$ at 600 °C [7], obviously, the H absorption and desorption behaviours are composition-dependent.

Significant improvement of the hydrogenation kinetics of the Mg-based alloys can be reached by application of melt spinning [8–10], as a result of nanostructuring. Such nanostructured alloys readily absorb and desorb ≈5 wt.% hydrogen during their cycling at lowered temperatures. These favorable features have been attributed to the enhanced hydrogen transport along the nanoboundaries [11].

The present work was aimed on the microstructural optimisation of the $LaMg_{12}$ alloy prepared by Rapid Solidification (RS), to better understand the dependence of the hydrogenation properties from the grain size and microstructure of the material. Hydrogenation sorption/desorption cycling and thermal desorption spectroscopy (TDS) were used to analyse the hydrogenation properties as related to the microstructure of the alloy studied by scanning electron microscopy (SEM) and by electron probe microanalysis (EPMA). Time-resolved synchrotron X-ray diffraction (SR XRD) was applied to monitor the metal–hydrogen interaction in the $LaMg_{12}$–H_2 system during the hydrogen absorption–desorption

* Corresponding author at: Institute for Energy Technology, Kjeller, NO 2027, Norway. Tel.: +47 63806453; fax: +47 63812905.
E-mail address: volodymyr.yartys@ife.no (V.A. Yartys).
[1] On leave from IPChPh Russian AS.

0925-8388/$ – see front matter © 2010 Elsevier B.V. All rights reserved.
doi:10.1016/j.jallcom.2010.09.172

cycling. This yielded high sensitivity in detecting formation of the phase constituents and excellent precision in refining the crystallographic parameters of the components.

2. Experimental details

2.1. Sample preparation and RS

$LaMg_{12}$ was synthesised from individual La and Mg metals in a vacuum-sealed steel crucible. The purity of the initial components was not less than 99.8%, and they were mixed in a stoichiometric 1:12 ratio. Melting was performed by placing an ampoule into a furnace kept at 750 °C for 30 min, and the ampoule was quenched into cold water afterwards. Rapid Solidification was applied to the as cast $LaMg_{12}$ alloy using a Cu wheel, being at ambient temperature, under Ar atmosphere at three different wheel rotation speeds. Thickness of the obtained ribbon was in the range from 50 μm for the sample synthesized at 2000 rpm to 200 μm for the material obtained at 300 rpm. For the SR XRD studies, the ribbons were crushed into powder, which was filled into the quartz capillaries. Microstructures of the ribbons solidified at 300 and 1000 rpm exhibited texture. In contrast, microstructural investigations of the alloy solidified at 2000 rpm showed its complete homogeneity in the whole body of the sample.

2.2. Hydrogen absorption/desorption and temperature desorption spectroscopy (TDS)

Hydrogen desorption–absorption experiments were performed in a conventional Sieverts type apparatus. Characterisations of the reversible hydrogen storage capacity and the reaction kinetics were done by measuring pressure changes in a closed system with a calibrated volume. Hydrogenation was performed at 350 °C at a 20 bar H_2 pressure. Five hydrogen absorption/desorption cycles were performed. TDS data was collected starting from a pressure of 10^{-5} mbar at room temperature by heating the hydrogenated sample to 450 °C, using a constant heating rate of 2 °C/min.

2.3. SR XRD, SEM and EPMA

SEM and EPMA data were collected with a JEOL JXA—8500F instrument. Samples were embedded into epoxy resin, grinded, polished with a diamond spray and coated with carbon to provide conductivity. SR XRD studies of the samples were performed at the Swiss–Norwegian Beam Lines at BM01A and BM01B stations, European Synchrotron Radiation Facility (ESRF), Grenoble, France.

The measurements were performed using a setup designed for *in situ* studies of the chemical processes occurring in hydrogen gas or in vacuum ([12] and references therein). A small amount of the sample was put into a 0.5 mm quartz glass capillary (0.01 mm wall thickness), filling approximately 3–5 mm of the capillary. The capillary was seal-proof connected to the gaseous system using a carbon ferrule and a T-piece; the latter was attached to the goniometer head. Vacuum was created using a turbomolecular vacuum pump.

Experimental data at BM01A was collected using a MAR2300 image plate detector. The wavelength ($\lambda = 0.7350(1)$ Å) and sample-to-detector distance ($d = 200$ mm, giving a usable range of d-spacing of 1.06–21 Å ($2\theta = 2$–$40.5°$)) were calibrated using LaB_6 as a reference material. Collection of the diffraction data proceeded for 10 s; the time of the processing of the image-plate data was 53 s, giving a total time for a single measured data set of 63 s.

The diffractometer at station BM01B (Si(1 1 1) channel-cut monochromator, scintillation detectors) is equipped with six counting chains, with an angular offset in 2θ of 1.1°. For in situ measurements the detector bank is moved by 1.2° during one measurement, and the data from the six different detectors are bound into one set. One data set ($2\theta = 6.07$–$12.67°$) was collected in 3 min, using a wavelength of 0.5009(1) Å.

3. Results

3.1. As cast $LaMg_{12}$

From the SEM study, the as cast $LaMg_{12}$ alloy contained two main constituents; $LaMg_{12-x}$ intermetallic alloy (approximately 80%) and an eutectic mixture of $LaMg_{12-x}$ and Mg (~20%). The $LaMg_{12-x}$ alloy forms large grains with an average size of 100–200 μm and, according to the EPMA analysis, had the composition $LaMg_{11.7}$. Eutectic part of the microstructure had a very fine lamellar morphology (see Fig. 1).

XRD analysis showed the formation of trace amounts of secondary phases, including La_2Mg_{17} and $LaMg_3$, in addition to $LaMg_{11.7}$ and Mg.

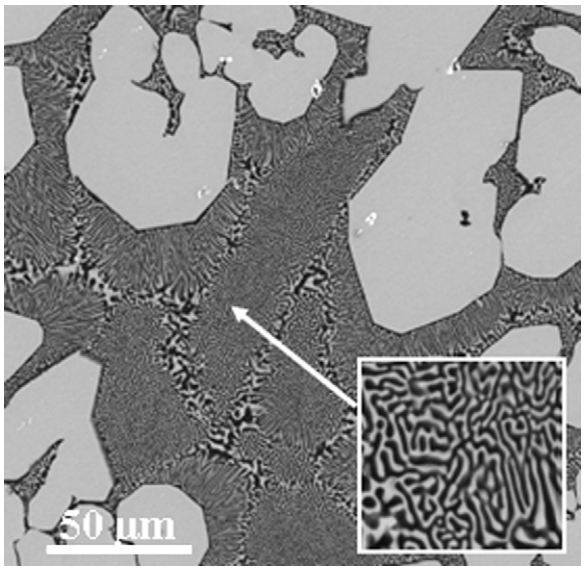

Fig. 1. Microstructure of the as cast La-Mg alloy showing large grains of the intermetallic phase $LaMg_{12-x}$ and a eutectic consisting of $LaMg_{12-x}$ and Mg. The inserted enlarged image has a side of rectangular area of 20 μm.

Formation of the Mg-deficient $LaMg_{\sim 11}$ structure was observed by the authors earlier during the hydrogen-assisted synthesis of this compound from lanthanum and magnesium [4]. Similarly, in the Ce–Mg system, the Mg-deficient $CeMg_{10.75-11.31}$ intermetallic is formed instead of the stoichiometric $CeMg_{12}$ compound [13].

The as cast alloy was used to synthesize the alloys with identical chemical composition but with a variable grain size. The Rapid Solidification technique was applied for this purpose. The quenching of the melt proceeded on a rotating copper wheel at velocities of 3.1, 10.5 and 20.9 m/s. Such velocities were achieved at 300, 1000 and 2000 rpm. Corresponding samples will further be referred to as RS300, RS1000 and RS2000 in the paper.

3.2. Rapidly solidified $LaMg_{12}$ alloys

Phase-structural analysis of the melt spun $LaMg_{12}$ alloys performed with the use of synchrotron X-ray diffraction showed that all alloys contained two phases: $LaMg_{12-x}$ intermetallic and Mg metal (Fig. 2 and Table 1). Depending on the solidification rate, the intermetallic alloy was found to form three polymorphic modifications. Two modifications of $LaMg_{12-x}$ were identified in the RS300 and RS1000 alloys, crystallized with a tetragonal $ThMn_{12}$-type and an orthorhombic $LaMg_{11}$ type of structure [4]. The latter structure, having a giant unit cell, is closely related to the $ThMn_{12}$-type structure and can be presented as a long range ordering of tetragonal $ThMn_{12}$-type subunits [4]. The quantity of the orthorhombic modification is highest at the lowest solidification rate (RS300). After Rapid Solidification at the highest applied quenching rate (RS2000), the alloy was partially amorphous, which was indicated by the presence of diffuse peaks in the SXRD pattern (most intensive at $2\theta \approx 11°$, see Fig. 2). Furthermore, and most interestingly, the alloy also contained a new intermetallic hexagonal $TbCu_7$-type of structure that has not earlier been reported for the $LaMg_{12-x}$ alloys.

The structural relationship between the three different modifications of $LaMg_{12-x}$ can easily be formalized if one considers them as being derivatives of a $CaCu_5$ type of compound. Indeed, a number of the related crystal structures can be derived from the hexagonal $CaCu_5$ type AB_5 intermetallic compound by a partial replacement of the larger A atoms by the pairs of smaller B atoms (B_2 dumbbells). The simplest case is when the hexagonal $TbCu_7$ type (sp. gr. *P6/mmm*) is derived from the $CaCu_5$ structure by a random *partial*

Table 1
Phase-structural characteristics of the melt spun $LaMg_{12}$ alloys and their hydrides obtained from Rietveld refinement of SR XRD data.

Material	Phase	Space group	Unit cell parameters (Å)			Quantity (wt.%)
			a	*b*	*c*	
Initial alloys						
RS300	O-$LaMg_{\sim 11}$	*Immm*	10.345(1)	10.353(1)	77.47(1)	53.5(3)
	T-$LaMg_{\sim 11}$	*I4/mmm*	10.3514(6)	–	5.9584(5)	28.2(3)
	Mg	*P6₃/mmc*	3.2097(1)	–	5.2095(4)	18.2(2)
RS1000	O-$LaMg_{\sim 11}$	*Immm*	10.34(–)	10.36(–)	77.5(–)	32.2(3)
	T-$LaMg_{\sim 11}$	*I4/mmm*	10.3523(3)	–	5.9598(3)	50.2(2)
	Mg	*P6₃/mmc*	3.2109(3)	–	5.2106(6)	17.6(2)
RS2000[a]	H-$LaMg_{\sim 11}$	*P6/mmm*	5.9617(3)	–	5.2153(5)	85.5(1)
	Mg	*P6₃/mmc*	3.211(1)	–	5.217(3)	14.5(3)
After 1st hydrogenation (350 °C, 20 bar H_2, 24 h)						
RS300 Hydr (H content ~3.0 wt.%)	α-MgH_2	*P4₂/mnm*	4.5150(3)	–	3.0185(3)	31.1(2)
	Mg	*P6₃/mmc*	3.2081(2)	–	5.2087(4)	40.3(2)
	LaH_3	*Fm-3m*	5.6150(1)	–	–	28.6(1)
RS1000 Hydr (H content ~3.0 wt.%)	α-MgH_2	*P4₂/mnm*	4.5124(3)	–	3.0179(3)	31.4(2)
	Mg	*P6₃/mmc*	3.2076(2)	–	5.2090(4)	40.5(2)
	LaH_3	*Fm-3m*	5.6117(2)	–	–	28.1(1)
RS2000 Hydr (H content ~2.1 wt.%)	α-MgH_2	*P4₂/mnm*	4.5131(3)	–	3.0179(3)	19.2(2)
	Mg	*P6₃/mmc*	3.2072(1)	–	5.2054(2)	52.3(1)
	LaH_3	*Fm-3m*	5.6100(1)	–	–	28.5(1)
After TDS in vacuum						
RS300 TDS	Mg	*P6₃/mmc*	3.2100(1)	–	5.2115(1)	69.4(1)
	LaH_{2+x}	*I4₁/amd*	5.6313(1)	–	11.3371(4)	29.1(1)
	T-$LaMg_{\sim 11}$	*I4/mmm*	10.348(2)	–	5.963(2)	1.5(1)
RS1000 TDS	O-$LaMg_{\sim 11}$	*Immm*	10.341(1)	10.359(1)	77.45(1)	65.8(2)
	T- $LaMg_{\sim 11}$	*I4/mmm*	10.338(1)	–	5.966(1)	21.8(4)
	Mg	*P6₃/mmc*	3.2092(2)	–	5.2098(7)	12.4(2)
RS2000 TDS	O-$LaMg_{\sim 11}$	*Immm*	10.3416(6)	10.3602(6)	77.510(5)	84.0(1)
	Mg	*P6₃/mmc*	3.2119(1)	–	5.2123(5)	16.0(2)

[a] The relative amounts of the crystalline phases in the alloys do not account for the presence of the amorphous component. Its content can be found from the quantitative Rietveld refinements of the XRD data for the studied samples with amorphous component, when these samples are mixed with a known amount of a crystalline reference material serving as an internal standard. Such experiments are planned in our future studies.

$B_2 \rightarrow A$ replacement [14]. The overall stoichiometry can be presented as $A_{1-x}B_{5+2x}$, *e.g.* the AB_{12} composition is achieved for $x = 1/2$ when 50% of A is replaced by B atoms. The initial hexagonal symmetry of the $CaCu_5$ type structure is retained and a new 2*e* site (B_2 dumbbell) is introduced in addition to the partially occupied 1*a* site (A).

The tetragonal $ThMn_{12}$ structure [15] is obtained from four hexagonal $AB_5/CaCu_5$-type subcells by an ordered replacement of half of the A atoms by pairs of B atoms; the B pairs being aligned along the hexagonal axis [16]. The metric relation between the hexagonal $TbCu_7$ ($CaCu_5$) and the tetragonal $ThMn_{12}$-type unit cells is as follows: $a_{tetr} = 2c_{hex}$; $c_{tetr} = a_{hex}$; $c_{tetr} \approx a_{tetr}/\sqrt{3}$.

Thus, the difference between the hexagonal $TbCu_7$ type and the tetragonal $ThMn_{12}$-type modifications of the $LaMg_{12-x}$ is in the extent of order between the La and Mg_2 pairs. In the tetragonal $ThMn_{12}$-type and orthorhombic $ThMn_{12}$-related structures the Mg_2 dumbbells have a long range order, whereas in the hexagonal $TbCu_7$-type structure a random distribution of Mg_2 pairs and La atoms takes place. Structural relations between the tetragonal $ThMn_{12}$ (sp. gr. *I4/mmm*) and orthorhombic $LaMg_{\sim 11}$ structures (sp. gr. *Immm*; $a_{orth} \approx b_{orth} \approx a_{tetr}$; $c_{orth} \approx 13c_{tetr}$) were considered in detail in our previous paper [4].

The presence of significant quantities of Mg in all the $LaMg_{12-x}$ alloys indicates that the stoichiometry of the intermetallic phase is $LaMg_{\sim 11}$ rather than $LaMg_{12}$. Deviation from the ideal 1:12 stoichiometry is explained by a partial $La \rightarrow Mg_2$ replacement (as has already been shown in [4]), thus some $La \leftrightarrow Mg_2$ disorder still exists in both *ordered* tetragonal and orthorhombic modifications.

Finally, the hexagonal $TbCu_7$-related modification of the $LaMg_{\sim 11}$ appears to be the least thermodynamically stable one of the three polymorphs. SR XRD study showed that after annealing of the RS2000 alloy at 500 °C, the $TbCu_7$-type structure and the amorphous material both transformed into the orthorhombic $LaMg_{12-x}$ polymorph, indicating that the latter phase had the highest thermodynamic stability of the three polymorphs.

3.3. Hydrogenation and thermal desorption spectroscopy studies

For all studied samples, the first hydrogenation was rather slow and was not completed after 12 h. Analysis of the SR XRD data of the hydrogenated materials showed complete disproportionation of the intermetallic $LaMg_{\sim 11}$ phase with the formation of LaH_3 and MgH_2. In addition, a significant quantity of the unhydrogenated Mg phase was also observed (see Table 1). Cycling of hydrogen absorption and desorption significantly increased the rate of hydrogen uptake for all studied materials and changed the kinetics of H uptake. Indeed, the curves of the 5th hydrogenation could be separated into a "fast" and a "slow" part, while the first hydrogenation did not show any rapid absorption at all.

The behaviour of the RS2000 sample was very different from the RS300 and RS1000 alloys. The two latter materials showed a drop in hydrogen capacity upon cycling, see Fig. 3, while the RS2000 alloy, in contrast, demonstrated an improvement in the H storage performance upon cycling and reached the storage capacity of 5.77 wt.% H after the 5th cycle.

A detailed *in situ* SR XRD study of the hydrogenation of the $LaMg_{12}$ alloy (350 °C; 20 bar H_2) showed that a two-stage hydrogen absorption took place (Fig. 4). How the XRD spectrum from the alloy during hydrogenation changed with time is shown in Fig. 4. No evidences of the formation of an interstitial $LaMg_{\sim 11}H_x$ hydride

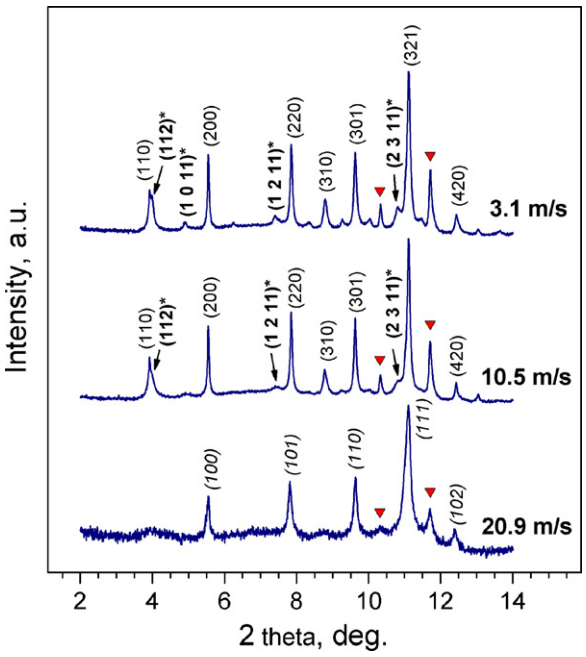

Fig. 2. Synchrotron X-ray powder diffraction patterns (λ = 0.5009 Å) of the $LaMg_{12}$ alloy solidified at different speeds of the copper wheel. Peaks of Mg metal are shown by triangles. Reflections from the $LaMg_{12-x}$ phase are shown with Miller indices corresponding to the three different observed structure modifications: hexagonal (italic font), tetragonal (plain font) and orthorhombic (bold with asterisk). We note that at the highest solidification rate, $LaMg_{12-x}$ crystallizes in the hexagonal $TbCu_7$ type structure, while at the lower cooling rates, both tetragonal ($ThMn_{12}$ type) and orthorhombic ($LaMg_{11}$ type) structure modifications are formed. For the orthorhombic structure, only the strongest "superstructure" peaks, not overlapping with those of the tetragonal modification, are identified.

was observed. In contrast, at the beginning of the hydrogenation process, the reflections from a cubic LaH_3 hydride appeared, with a simultaneous growth of the Mg peaks (as mentioned earlier, some amount of Mg metal was present already in the initial alloy), and the peaks of the $LaMg_{\sim 11}$ intermetallic decreased in intensities. After approximately 15 min of hydrogenation, only the peaks from LaH_3 and Mg phases could be identified in the diffraction pattern. This confirms the completeness of the disproportionation of the intermetallic compound. On further hydrogenation, the appearance and slow growth of the MgH_2 peaks can be seen. Thus, two consecutive steps of the hydrogenation process took place:

(1) Disproportionation reaction: $LaMg_{12-x} + 3/2H_2 \rightarrow LaH_3 + (12-x)Mg$
(2) Hydrogenation of the formed Mg: $Mg + H_2 \rightarrow MgH_2$.

Quantitative analysis of the *in situ* SR XRD data by the Rietveld profile refinements allowed an estimation of the kinetics of these hydrogenation stages (Fig. 5). In the applied conditions the rate of the LaH_3 formation ($LaMg_{12-x}$ disproportionation) was about 30 times higher than the rate of the formation of MgH_2. Similar hydrogenation behaviour has also been observed for the Mg-rich yttrium intermetallic Y_5Mg_{24} [17].

TDS of the hydrogenated RS samples showed significant differences between the behaviour of the RS300 hydride on one hand, and the RS1000 and RS2000 hydrides on the other hand (see Fig. 6). In addition to the main event of hydrogen desorption at 357–375 °C, the two latter hydrides exhibited an extra desorption peak at 415 °C. From an *in situ* SR XRD study of the hydrogenated RS1000 alloy, it was found that thermal hydrogen desorption proceeded in three steps. Following the temperature increase, two parallel trans-

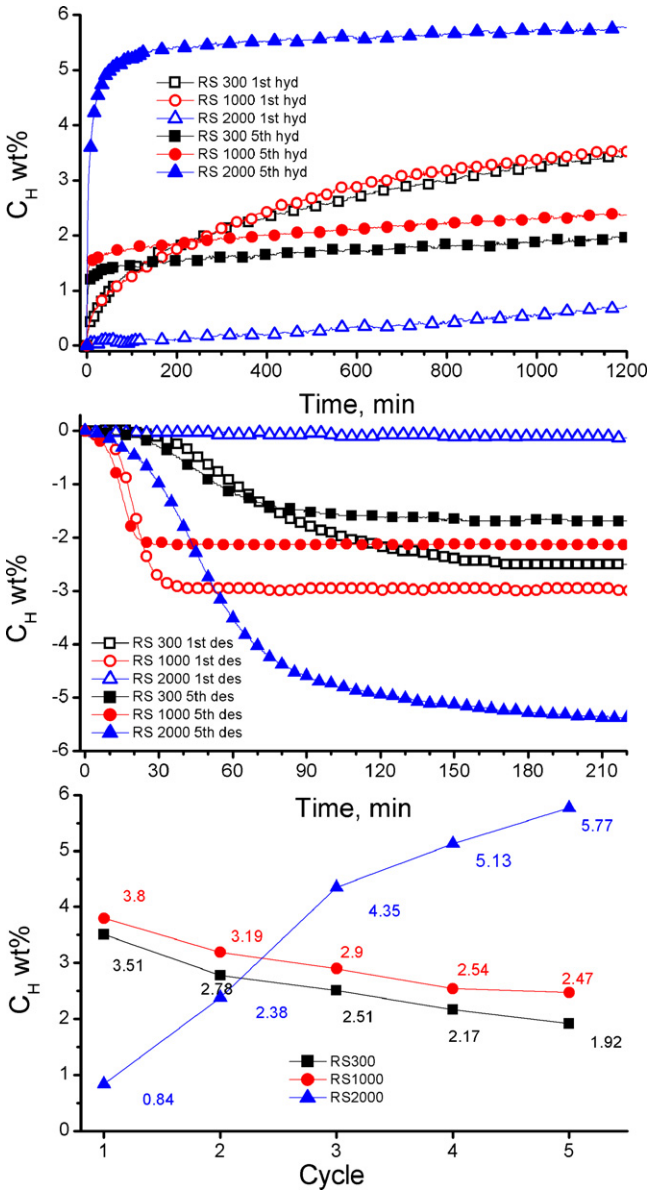

Fig. 3. Hydrogen absorption–desorption of RS $LaMg_{12}$ alloys during cycling at 350 °C: (a) absorption at 20 bar H_2; (b) desorption at ~1.5 bar H_2; (c) changes in the reversible H capacity upon cycling.

formations $LaH_3 \rightarrow LaH_2 + 1/2H_2$ and $MgH_2 \rightarrow Mg + H_2$ took place. These two overlapping steps manifested themselves by the most significant desorption peak in the TDS spectrum (at 357–375 °C). The second observed in the TDS desorption peak at 415 °C was identified as a Mg-assisted decomposition of LaH_2, which proceeds at a temperature that is 400 °C lower than the decomposition of La dihydride, and leads to a recombination of $LaMg_{12-x}$. This recombination took place only for the RS1000 and RS2000 samples. For the RS300 hydride, the LaH_2 dihydride was not destabilised at the experimentally applied temperatures below 475 °C. Thus, the recombination process did not take place. The data from the SR XRD studies of the samples after the TDS experiments are presented in Fig. 7 and Table 1. The recombined $LaMg_{12-x}$ intermetallic was found to crystallise in its orthorhombic polymorphic modification.

Below we will present the results of the microstructural characterisation of the studied materials, which completely support the proposed scheme of interaction.

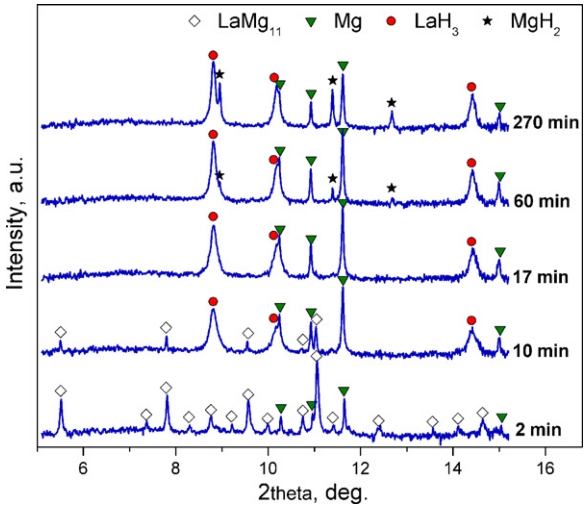

Fig. 4. Evolution of the SXRD pattern (λ = 0.5009 Å) of the $LaMg_{12}$ alloy during *in situ* hydrogenation at 350 °C and 20.5 bar H_2. Time from the beginning of the hydrogenation process is given for each spectrum.

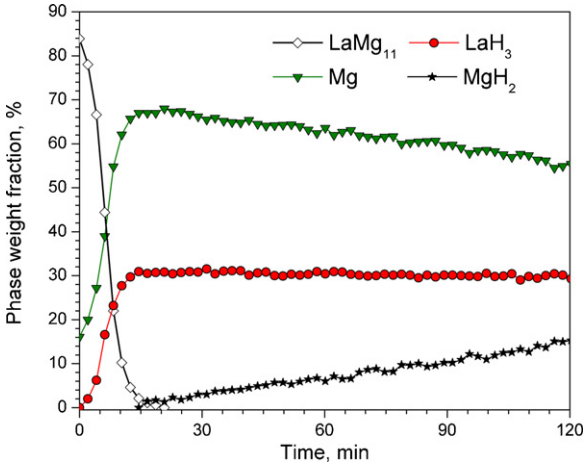

Fig. 5. Changes in phase composition of the $LaMg_{12}$ alloy during the hydrogenation process, obtained from the Rietveld profile refinements of the *in situ* SXRD data. We note that a complete disproportionation of the $LaMg_{11}$ intermetallic compound into LaH_3 and Mg occurs within ~15 min from the start of the hydrogenation process; it is followed by a much slower $Mg \rightarrow MgH_2$ transformation (after 270 min of hydrogenation only 40% of Mg is converted into the corresponding hydride).

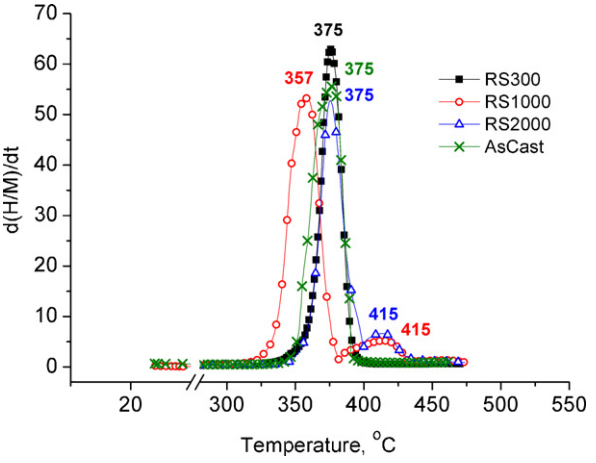

Fig. 6. Hydrogen vacuum thermal desorption spectra of the hydrogenated RS alloys (heating rate 2 °C/min).

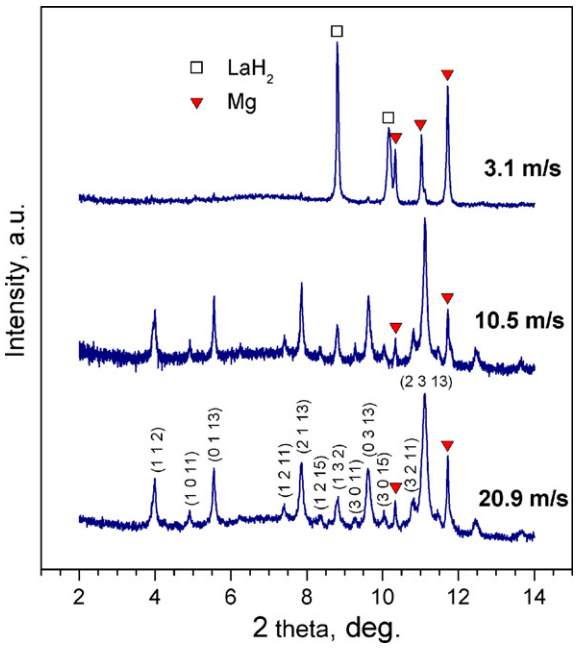

Fig. 7. Synchrotron X-ray powder diffraction patterns (λ = 0.5009 Å) of the rapidly solidified $LaMg_{12}$ alloys after vacuum thermal desorption from their corresponding hydrides (TDS experiment). Miller indices of the strongest reflections of the orthorhombic $LaMg_{11}$ structure (sp. gr. *Immm*; *a* = 10.34, *b* = 10.36, *c* = 77.5 Å) are shown.

Similar to the RS300 hydride, the hydrogenated as cast alloy also did not recombine during the TDS to produce $LaMg_{12-x}$. These similarities are probably related to the large particle sizes of the phase constituents in the as cast alloy and the RS300 material, in contrast to the fine microstructures of the RS1000 and RS2000 alloys.

SEM studies showed that the changes in quenching rate during the Rapid Solidification process greatly influenced the microstructures of the materials (see Fig. 8). The RS300 and RS1000 materials formed similar microstructures containing extensive dendrite areas, up to ~50% of the sample in the RS1000 alloy. In contrast, the RS2000 ribbons contained nanocrystalline particles in an amorphous matrix.

Ribbons of the RS samples retained their initial shapes after the hydrogenation (despite the fact that formation of LaH_3 and MgH_2 hydrides is accompanied by a significant volume expansion) and showed formation of MgH_2 particles on the surfaces (Fig. 8). The size of the MgH_2 surface-particles increased with increasing solidification rate. Indeed, for RS300, the MgH_2 particles were in the range from 0.2 to 1 μm. In addition to that, growing from the surface, long needle-type MgH_2 rods (whiskers) were observed. Similar whiskers were also observed in [17]. In contrast, in the RS1000 and RS2000 alloys the hydride particle size was much larger, up to 3 μm. No MgH_2-based nano-whiskers were formed in these samples.

The SEM studies revealed significant differences between the samples after completion of the hydrogen thermal desorption. Samples RS1000 and RS2000 were found to be very porous (pore sizes 0.5–2 μm), while RS300 remained intact (Fig. 8). Such differences in morphology can be attributed to the recombination of the $LaMg_{12-x}$ intermetallic in the RS1000 and RS2000 samples on H desorption and associated with volume shrinkage during the $Mg + LaH_2 \rightarrow LaMg_{\sim 11}$ transformation. No such transformation took place in the RS300 and as cast samples, so internal volume collapse did not take place, and no cavities are formed.

The chemical equations of these two processes can be described as follows:

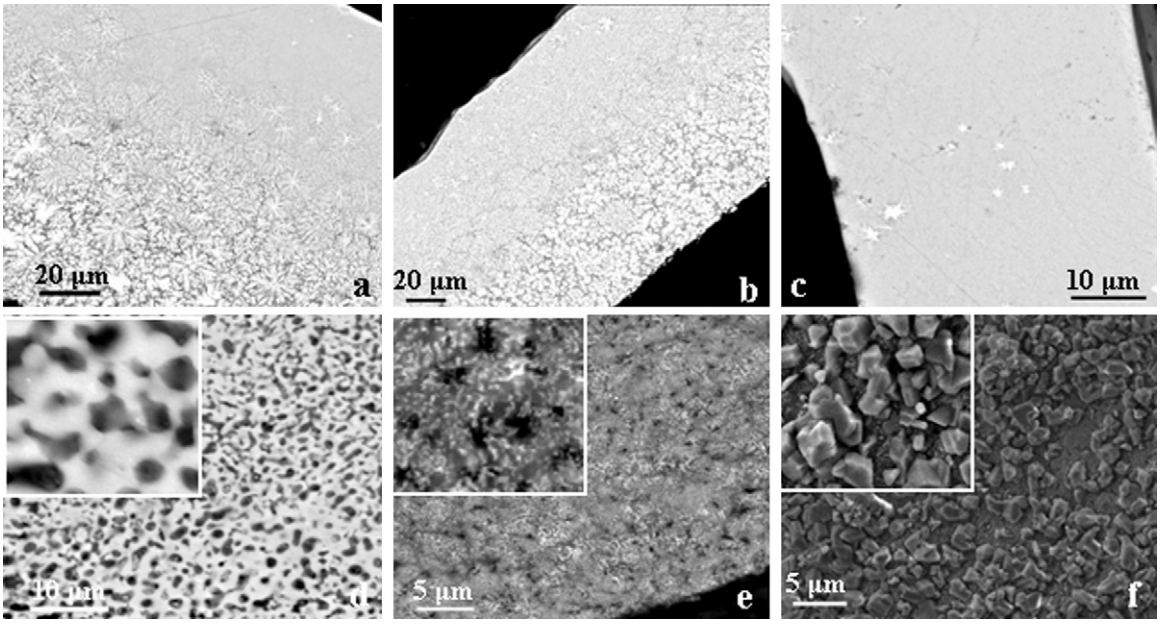

Fig. 8. Backscattered SEM images of the RS $LaMg_{12}$ samples (a, RS300; b, RS1000; c, RS2000) and RS2000 sample at different stages of hydrogen processing (d, after TDS from the hydride; e, after 5 hydrogen absorption–desorption cycles; f, hydrogenated sample). For the inserted magnified square area its sides are 5 μm.

1 *Desorption without a recombination* (*RS300 and as cast samples*)

$$MgH_2 + LaH_3 \rightarrow Mg + LaH_2 + H_2$$

2 *Desorption followed by recombination of* $LaMg_{\sim 11}$ (*RS1000 and RS2000*)

$$MgH_2 + LaH_3 \rightarrow Mg + LaH_2 + H_2 \rightarrow LaMg_{12-x} + H_2.$$

4. Summary and conclusions

In the present work, the microstructural modification of the $LaMg_{12}$ alloy was performed by means of the Rapid Solidification technique. The structure and microstructure of the alloys were closely related to the solidification rate. Three types of the parent crystal structures, including, for the first time reported for the La–Mg alloys, hexagonal $TbCu_7$ type, together with the earlier known tetragonal $ThMn_{12}$ and orthorhombic $LaMg_{11}$ types, were revealed during the SR XRD studies of the alloys. Detailed mechanisms of hydrogen absorption and desorption were studied. The process of hydrogenation occurred in two steps studied in detail by *in situ* SR XRD. As the first step, a decomposition of $LaMg_{12}$ into LaH_3 and Mg occurred and, only after that, MgH_2 was formed. RS300 and RS1000 alloys both showed higher rates of hydrogen exchange; and thus, already during the first cycles, the H storage capacities reached ~70% of the maximum level. However, at the same time, a decrease in the H storage capacity during the cycling was observed. The RS2000 alloy was, in spite of the low hydrogen absorption and desorption rates in the very first cycle, completely saturated by hydrogen already during its 5th hydrogenation and was maintaining its maximum H storage capacity during the following absorption–desorption cycling. The reason for such differences in behaviour is the differences in the initial microstructure and the grain size of the alloys caused by the Rapid Solidification. SEM studies showed a clear difference between the RS300 and RS2000 samples, the latter containing nano-grains and partially amorphous structures.

The desorption process from the hydrogenated materials resulted in the decomposition of MgH_2 and a partial hydrogen desorption from LaH_3 to form LaH_{2+x}. Thermal desorption in vacuum occurred in different ways for the three alloys and resulted in a complete recombination of the $LaMg_{12-x}$ intermetallic for RS1000 and RS2000. Such a recombination was not observed for the RS300 ribbon and the hydrogenated as cast alloy, which is attributed to their coarse initial microstructures. After TDS, samples RS1000 and RS2000 were very porous (pore sizes 0.5–2 μm), which can be associated with volume shrinking when the $Mg + LaH_2 \rightarrow LaMg_{\sim 11}$ transformation occurred during the recombination of the $LaMg_{12-x}$ intermetallic. These observations allow us to conclude that fine nanostructuring of the material leads to a complete recombination process and to the enhancement of hydrogen exchange. Thus, Rapid Solidification proves to be an efficient route in favourably modifying of the hydrogenation behaviour of the intermetallics of rare earth metals and magnesium.

Acknowledgements

The authors are grateful to the staff of the Swiss-Norwegian Beam Lines, Grenoble, for their skilful assistance in the SR XRD experiments. Dr. Jan Petter Mæhlen is sincerely thanked for the help in the work. Many thanks go to Jan Arve Båtnes (NTNU) and Harald Holm (NTNU) for their assistance with Rapid Solidification equipment.

References

[1] K. Pal, Int. J. Hydrogen Energy 22 (8) (1997) 799–804.
[2] D. Sun, F. Gingl, Y. Nakamura, H. Enoki, M. Bououdina, E. Akiba, J. Alloys Compd. 333 (2002) 103–108.
[3] X.P. Gao, Y. Wang, Z.W. Lu, W.K. Hu, F. Wu, D.Y. Song, P.W. Shen, Chem. Mater. 16 (13) (2004) 2515–2517.
[4] R.V. Denys, A.A. Poletaev, J.K. Solberg, B.P. Tarasov, V.A. Yartys, Acta Mater. 58 (7) (2010) 2510–2519.
[5] R.V. Denys, A.B. Riabov, J.P. Maehlen, M.V. Lototsky, J.K. Solberg, V.A. Yartys, Acta Mater. 57 (13) (2009) 3989–4000.
[6] V.A. Yartys, R.V. Denys, J.P. Maehlen, C.J. Webb, E. MacA. Gray, T. Blach, A.A. Poletaev, J.K. Solberg, O. Isnard, in: C.M. Wang, N. de Jonge, R.E. Dunin-Borkowski, A. Braun, J.-H. Guo, H. Schober, R.E. Winans (Eds.), Mater. Res. Soc. Symp. Proc., vol. 1262, Warrendale, PA, 2010, 1262-W04-01, ISBN:978-1-60511-239-8, Proceedings of the 2010 MRS Spring Meeting, San Francisco, USA, 5–9 April 2010.
[7] B. Darriet, M. Pezat, A. Hbika, P. Hagenmuller, Mater. Res. Bull. 14 (1979) 377–385.

[8] K. Tanaka, Y. Kanda, M. Furubayashi, K. Saito, K. Kuroda, H. Saka, J. Alloys Compd. 293–295 (1999) 521–525.
[9] J. Yin, K. Tanaka, N. Tanaka, Mater. Trans. 43 (2002) 417–420.
[10] J. Yin, K. Tanaka, Mater. Trans. 43 (2002) 1732–1736.
[11] K. Tanaka, J. Alloys Compd. 450 (2008) 432–439.
[12] J.P. Maehlen, V.A. Yartys, R.V. Denys, M. Fichtner, Ch. Frommen, B.M. Bulychev, P. Pattison, H. Emerich, Y.E. Filinchuk, D. Chernyshov, J. Alloys Compd. 446–447 (2007) 280–289.
[13] X. Zhang, D. Kevorkov, J. Alloys Compd. 475 (2009) 361–367.
[14] K.H.J. Buschow, A.S. Van der Goot, Acta Crystallogr. 27B (1971) 1085–1088.
[15] J.V. Florio, R.E. Rundle, A.I. Snow, Acta Crystallogr. 5 (1952) 449–457.
[16] J.V. Florio, N.C. Baenziger, R.E. Rudle, Acta Crystallogr. 9 (1956) 367–372.
[17] C. Zlotea, J. Lu, Y. Andersson, J. Alloys Compd. 426 (2006) 357–362.